Journal of Geophysical Research: Space Physics

RESEARCH ARTICLE
10.1029/2018JA025486

ARTEMIS Observations of Solar Wind Proton Scattering off the Lunar Surface

C. Lue[1,2], J. S. Halekas[1], A. R. Poppe[3], and J. P. McFadden[3]

[1]Department of Physics and Astronomy, University of Iowa, Iowa City, IA, USA, [2]Swedish Institute of Space Physics, Kiruna, Sweden, [3]Space Sciences Laboratory, University of California, Berkeley, CA, USA

Key Points:
- Using ARTEMIS data, we observe lunar H^+ surface-scattering at $0.4^{\pm 0.1}$% of the incident H^+ flux
- Like scattered H atoms, scattered H^+ favors the backward direction
- The ratio of scattered H^+/H decreases with impact speed and increases with exit speed

Supporting Information:
- Supporting Information S1

Correspondence to:
C. Lue,
charles.lue@irf.se

Citation:
Lue, C., Halekas, J. S., Poppe, A. R., & McFadden, J. P. (2018). ARTEMIS observations of solar wind proton scattering off the lunar surface. *Journal of Geophysical Research: Space Physics*, *123*. https://doi.org/10.1029/2018JA025486

Received 19 MAR 2018
Accepted 16 JUN 2018
Accepted article online 26 JUN 2018

Abstract We study the scattering of solar wind protons off the lunar surface, using ion observations collected over 6 years by the ARTEMIS satellites at the Moon. We show the average scattered proton energy spectra, directional scattering distributions, and scattering efficiency, for different solar wind incidence angles and impact speeds. We find that the protons have a scattering distribution that is similar to existing empirical models for scattered hydrogen energetic neutral atoms, with a peak in the backward direction (toward the Sun). We provide a revised model for the scattered proton energy spectrum. We evaluate the positive to neutral charge state ratio by comparing the proton spectrum with existing models for scattered hydrogen. The positive to neutral ratio increases with increasing exit speed from the surface but decreases with increasing impact speed. Combined, these counteracting effects result in a scattering efficiency that decreases from ~0.5% at 300 km/s solar wind speed to ~0.3% at 600 km/s solar wind speed.

1. Introduction

Solar wind protons that impact the lunar surface may scatter and return to space at high energies. Most of these scattered protons capture an electron at the surface and thus become hydrogen energetic neutral atoms (H_{ENA}). Ten percent to 20% of the incident protons scatter as H_{ENA} with energies above 20 eV (McComas et al., 2009; Wieser et al., 2009), while ~0.1–1% of the incident protons scatter with a positive charge (H^+; Saito et al., 2008).

Scattered H_{ENA} have proven very useful for remote sensing of plasma precipitation onto the lunar surface. By using empirical models for the H_{ENA} scattering properties (e.g., Futaana et al., 2012; Schaufelberger et al., 2011), it is possible to remotely measure the precipitating plasma flux (Futaana et al., 2006) and flow speed (Futaana et al., 2013). Such measurements are of special interest wherever the plasma precipitation is modified at altitudes too low to directly measure with spacecraft, such as at the lunar magnetic anomalies (LMAs; Futaana et al., 2013; Harada et al., 2014; Lue et al., 2016; Saito et al., 2012; Wieser et al., 2010; Vorburger et al., 2012, 2013, 2015).

Scattered H^+ (just like H^+ reflected from LMAs, e.g., Lue et al., 2011; Poppe et al., 2017; Saito et al., 2010) are important for the lunar plasma environment. The ions interact with and perturb the ambient solar wind flow (Fatemi et al., 2014; Harada et al., 2014; Halekas et al., 2012, 2014, 2017). The ions travel on cycloid trajectories that can bring them thousands of kilometers upstream of the Moon (Futaana et al., 2003; Holmström et al., 2010), or give them access to the lunar wake and the night side surface (Fatemi et al., 2014; Futaana et al., 2010; Nishino et al., 2009; Vorburger et al., 2016).

In the present study, we investigate the scattering properties of H^+ scattered from the lunar regolith, as observed by the ion sensors on the two spacecrafts of the ongoing Acceleration, Reconnection, Turbulence, and Electrodynamics of the Moon's Interaction with the Sun (ARTEMIS) mission (Angelopoulos, 2010; Sibeck et al., 2011). We also study how the scattering properties vary with solar wind incidence angle and impact speed.

The study builds on previous work by Lue et al. (2014) that used a few weeks of data from the Chandrayaan-1 lunar satellite at low solar-zenith angles (*SZA*s) and scattering directions close to the Zenith. Here we use a much larger data set to reassess the H^+ energy spectrum and the scattering rate as a function of the impact speed. In addition, we investigate the H^+ directional scattering distribution.

2. Instrumentation and Data

To measure the scattered H^+, we use the Ion Electrostatic Analyzer (iESA; McFadden et al., 2008) on each ARTEMIS probe (P1 and P2). The ARTEMIS probes are placed in highly elliptical, near equatorial lunar orbits.

The aposelenes are at ~19,000 km, and the periselenes vary between 20 and 200 km. The corresponding orbit period is ~26 hr. The iESA has an energy range of 1.6 to 25 keV with an energy resolution of ΔE/E of 32% in the "Full" measurement mode used herein. The instrument field of view is $180^{o} \times 6°$ FWHM, where the 180° span is perpendicular to the spacecraft spin plane and separated into 16 anodes with 5.6° to 22.5° (higher resolution in the spin plane). With each spacecraft spin (every 3 s), the measurement covers the full angular space (4π sr). In the used mode, the data collection over the spin provides an angular resolution in the direction of spin of 22.5°. We selected the "Full" mode to get regularly collected data at high energy and angular resolution. A "Full" data package of 32 energy bins × 88 directional bins is measured over a single spin once every 32 or 128 spins.

For this study, we limit the data set to data packages obtained at lower than 300 km altitude, that is, near the periapsis. We do this to reduce the uncertainty in the back tracing of the measured fluxes to their inferred source points on the Moon (see next section). We also limit the data to times when the Moon is in the solar wind, outside of the terrestrial bow shock. The data retrieved for this study spans the period from July 2011 to May 2017.

The spacecraft stores onboard-calculated moment data based on their suites of plasma particle instruments including iESA. In this study, we use these derived moments (each time using the same probe that is used to observe the scattered H^{+}) to locally monitor the incident solar wind parameters. Further, we use magnetic field data collected by the Flux Gate Magnetometer (Auster et al., 2009) to monitor the interplanetary magnetic field.

3. Analysis

Each data package used in the study is analyzed by first back tracing the inferred ion trajectory that corresponds to each energy-direction bin of the package. The back tracing is solved analytically and accounts for the interplanetary magnetic field and the convection electric field of the solar wind. We discard any data corresponding to traces that do not intersect the lunar surface within a 300-km trace length. Furthermore, we discard any traces that intersect magnetized (LMA) regions of the lunar surface. An example of valid traces from a single data package is shown in Figures 1a and 1b.

We define the LMA regions with the help of Purucker and Nicholas's (2010) model of the crustal field strength. We use their model results for the crustal field strength map at 30 km altitude ("correlative model" ASCII table retrieved from http://core2.gsfc.nasa.gov/research/purucker/moon_2010) and we consider values of >2 nT given by this map to qualify as LMAs. We then add a padding of 152 km (corresponding to 5° latitude) to these regions. The padding is added to allow a certain uncertainty in the back tracing, as well as an uncertainty in the effective area-of-influence of the LMAs relative to their crustal location (the area shielded by an LMA may, e.g., be shifted downstream relative to the solar wind flow; c.f. Deca et al., 2015; Lue et al., 2016; Zimmerman et al., 2015). The resulting regions are comparable to maps of LMA-reflected H^{+} observations (Lue et al., 2011; Poppe et al., 2014, 2017).

Each successful trace to the unmagnetized lunar surface yields a recording of the corresponding at-surface differential flux and energy, both of which may differ from the at-spacecraft values due to acceleration along the trajectory (c.f. Figure 1c). We also record the *SZA* of the scattering point and the scattering azimuth and elevation, defined as shown in Figure 1d. The *SZA* is approximately equivalent to the solar wind incidence angle to the macroscopic surface normal (neglecting surface topography and microscopic roughness). From a single data package, a good estimate of the H^{+} energy spectrum can be obtained (Figure 1c), but only a limited part of the scattering distribution is obtained (Figure 1e).

To produce the energy spectrum, we subtract a constant instrument background count of 0.03 counts per bin per package. Further, we discard any traces that return a difference between the at-spacecraft and at-surface energy of a factor 1.5, to reduce the impact of incorrectly back tracing a background signal or non-H^{+} ion signal. For the energy spectrum, we ignore the scattering angles information when averaging the measurements.

For the scattering distribution, we produce an energy spectrum for each direction bin, and then integrate the spectrum trapezoidally under the condition that the spectrum is represented by at least three energy bins containing a positive differential flux estimate. Thus, many data packages must be accumulated to reliably reproduce the scattering distribution.

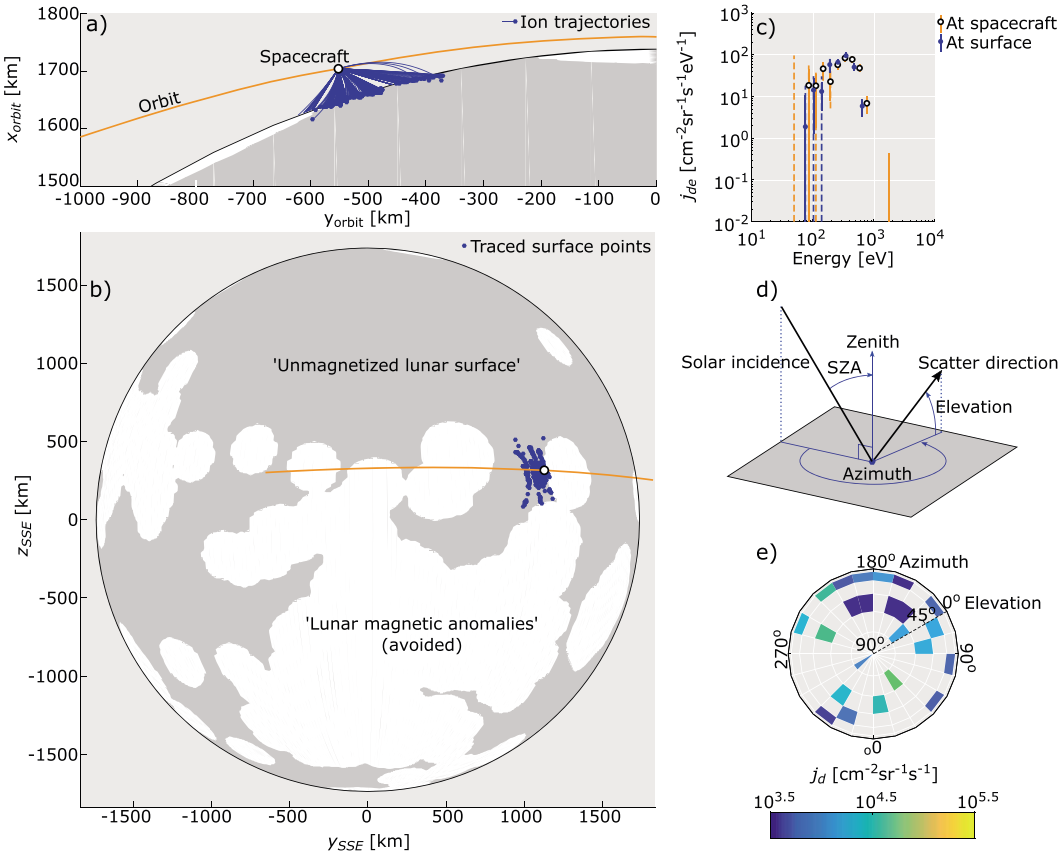

Figure 1. Analysis example of ARTEMIS iESA observations of scattered protons from the Moon for a single data package from 26 November 2011 10:16:06. After back-tracing the proton trajectories from the spacecraft, those trajectories with a <300-km trace path to a point on the unmagnetized lunar surface are recorded. Panel (a) shows these traced ion trajectories between the spacecraft and the surface source points. Panel (b) shows the source points on the lunar surface. The white regions in panels (a) and (b) show the locations of the lunar magnetic anomaly (LMA) regions. The LMA regions are avoided in this study. The coordinate system in panels (a) and (b) is selenocentric solar ecliptic (SSE). Note that the LMA regions rotate in this frame according to the lunar phase, and that the shown example is near New Moon. Panel (c) shows the proton energy spectrum (given in differential flux, j_{de}) as measured at the spacecraft and as inferred at the surface point according to the tracing. Solid lines in panel c indicate the standard error of the mean based on measurement variance and dashed lines indicate the Poisson error estimate (accounting for background count reduction), visible only where it is the greater error estimate. Panel (d) shows the definition of the scattering angles (azimuth, elevation, *SZA*) used herein, where *SZA* is the solar-zenith angle. Panel (e) shows the inferred scattering directions and directional fluxes (j_d) at the surface for the measured particles.

For the results presented in the next section, we accumulate analysis results for the whole 6-year data set, binned into different incidence angle and impact speed cases. To combine observations obtained over various solar wind flux conditions, we scale each measurement by a factor corresponding to a nominal solar wind flux of 10^8 cm^{-2} s^{-1} divided by the incident flux at the point and time of measurement. We do not show results for >75° *SZA* herein because of increasing influence of LMA-associated H^+, but these results are included in the supporting information for the paper.

Limiting the allowed ion acceleration along each traced trajectory to a factor < 1.5 effectively removes pick-up ion measurements, which otherwise appears along the convection electric field direction, at energies <~100 eV (c.f. Poppe et al., 2012). In addition, a sporadic but high-flux population appears near the solar wind energy (presumed to be LMA-reflected H^+ (c.f. Poppe et al., 2017) that sometimes are observed despite our efforts to avoid LMA regions). To remove the latter population, we exclude measurements of anomalously high fluxes from the surface (threshold set to 3,000 cm^{-2} sr^{-1} s^{-1} eV^{-1}).

4. Results

The average scattered H^+ energy spectra and directional distributions, for 15 parameter bins (three incidence angle bins and five impact speed bins) are shown in Figures 2 and 3. Results from the full range of 6 × 9 bins

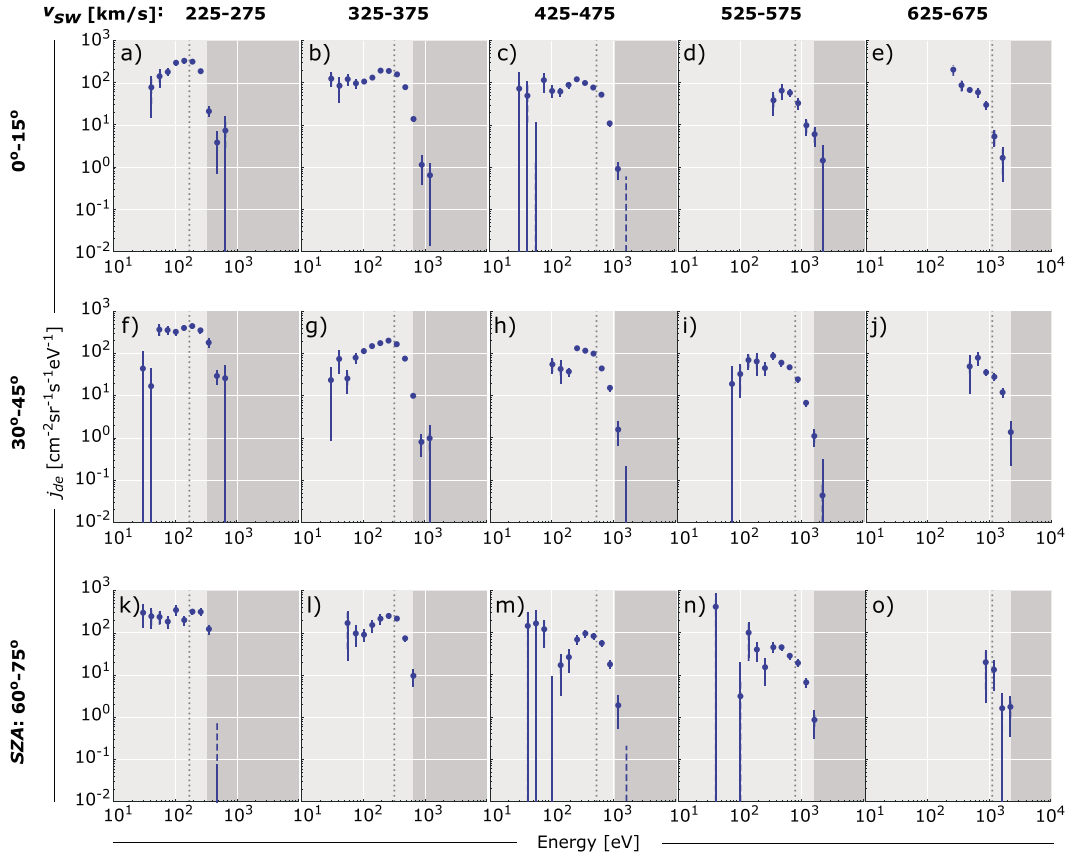

Figure 2. Scattered proton energy spectra of inferred differential flux (j_{de}) at the traced source point on the lunar surface, averaged over all data used in this study, separated into parameter bins with respect to solar wind speed (v_{sw}) and solar-zenith angle (*SZA*). The error bars are defined as in Figure 1. The dark shaded regions represent energies above the mean solar wind incidence energy, and the dotted vertical lines represent 50% of the latter value.

are available in the supporting information. In Figure 2, we see that the scattered H^+ spectra peak at a fraction of the solar wind impact energy and decrease rapidly near the impact energy. The ratio between the spectral peak and the impact energy decreases from ~1/2 at ~250 km/s to ~1/4 at ~550 km/s. The results for different incidence angles are consistent with each other given the error estimates. In other words, there is no clear dependence on the incidence angle.

In Figure 3, we see a clear change of the scattering distribution with increasing *SZA*. The distribution goes from nearly uniform at normal incidence ($SZA < 15°$) to a backward-directed scattering peak at high *SZA*. The statistics are not sufficient to distinguish a change in the scattering distribution with impact speed, other than an overall decrease in the scattering rate, examined further below.

In Figure 4, we investigate how the flux of scattered H^+ in relation to the incident H^+ flux, that is, the scattering efficiency, changes with incidence angle, and impact speed. We use two different methods: integrating the energy spectra (Figure 2) over energy, effectively assuming an isotropic scattering distribution (Method 1) and integrating the scattering distribution (Figure 3) over scattering solid angle (Method 2). Overall, the results are consistent with a scattering efficiency of $0.4^{\pm 0.1}$%. A decreasing trend of the scattering efficiency with increasing solar wind speed is observed, from ~0.5% to ~0.3%. Given the error estimates shown in Figure 4, there is no statistically significant dependence of the scattering efficiency on the incidence angle. Results for other incidence angle bins are included in the supporting information.

In Figure 5, we collapse the incidence angle separation of Figure 2 and show the average energy spectra, allowing incidence angles of 0°–75° *SZA* for five impact speed bins (results for intermediate bins are available in the supporting information). We compare the results with models for the H_{ENA} energy spectrum (F2012;

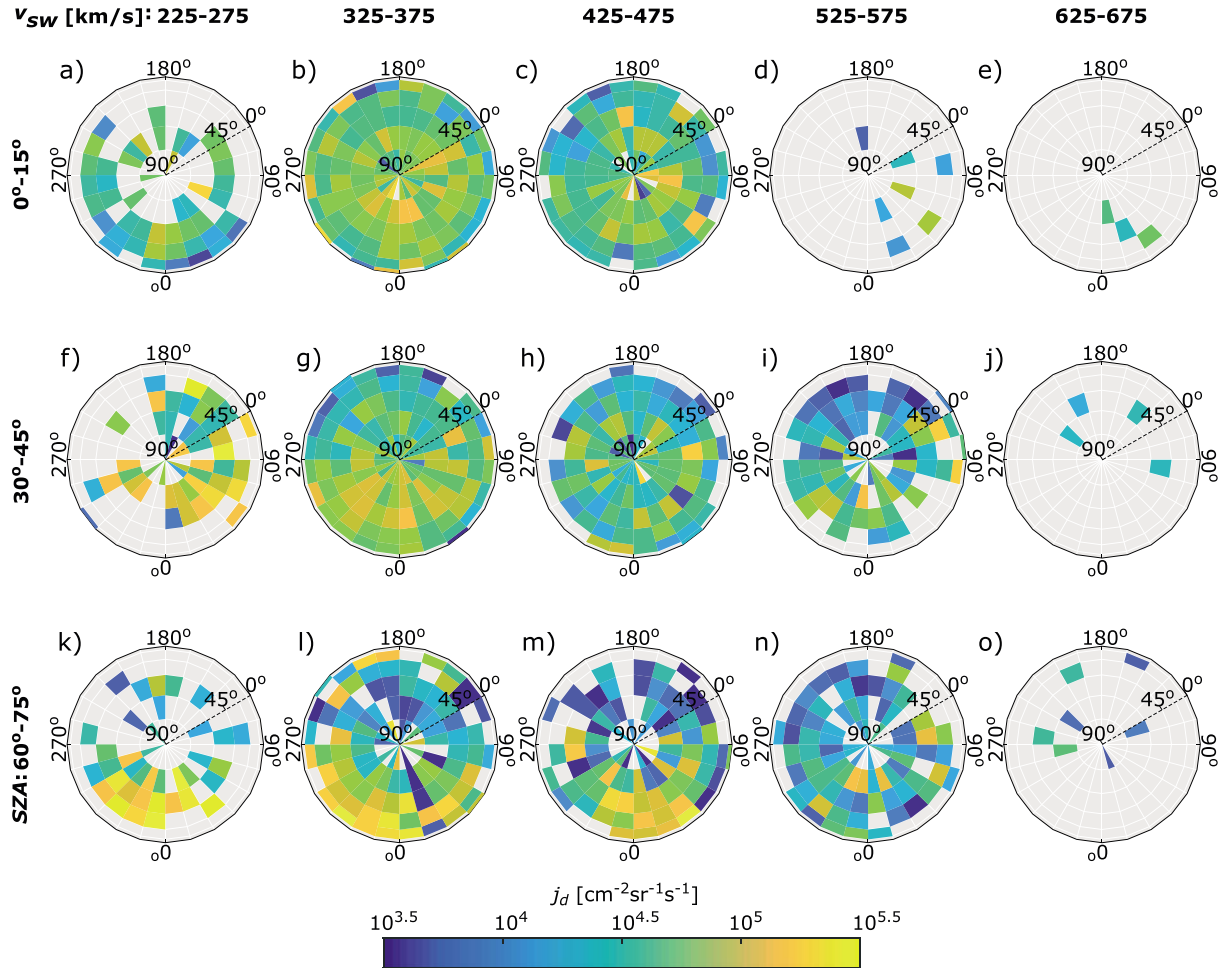

Figure 3. Proton scattering distributions in directional flux (j_d) illustrated in the same way as in Figure 1e, averaged over all data used in this study, separated into parameter bins with respect to solar wind speed (v_{sw}) and solar-zenith angle (*SZA*).

Futaana et al., 2012) and the previous model for the H^+ energy spectrum (L2014; Lue et al., 2014). The L2014 model is a convolution of the H_{ENA} velocity distribution and an exit speed dependence of the positive charge fraction:

$$f(v_{exit}) \propto \exp\left(\frac{-m_p v_{exit}^2}{2kT_{ENA}}\right) \cdot \exp\left(\frac{-v_c}{v_{exit}}\right),$$

where m_p is the proton mass, v_{exit} is the H^+ exit speed, kT_{ENA} is the characteristic H_{ENA} spectrum width; and v_c is the characteristic charge-exchange velocity. We refit the model to our observations, by a standard error-weighted least-square fitting of the parameters kT_{ENA} and v_c. While Lue et al. (2014) used a free scaling factor for fitting their results, we here set the model to be consistent with the H_{ENA} scattering efficiency at 20%, such that our model becomes

$$j_{dH+}(E_{exit}) = j_{dHENA}(E_{exit}) \cdot \exp\left(\frac{-v_c}{v_{exit}}\right) = \frac{0.2 \cdot J_{in}}{2\pi} \cdot \frac{E_{exit}}{kT_{ENA}^2} \cdot \exp\left(\frac{-E_{exit}}{kT_{ENA}}\right) \cdot \exp\left(\frac{-v_c}{v_{exit}}\right),$$

where j_{de} is the differential flux (particle number flux within a given directional solid angle and energy span). Note that the division by 2π here approximates the scattering as isotropic. To use the model for specific scattering directions, this quantity should be replaced accordingly (see the directional scattering model later herein). The refitted models seen in Figure 5 reproduce the main features of the observations, though

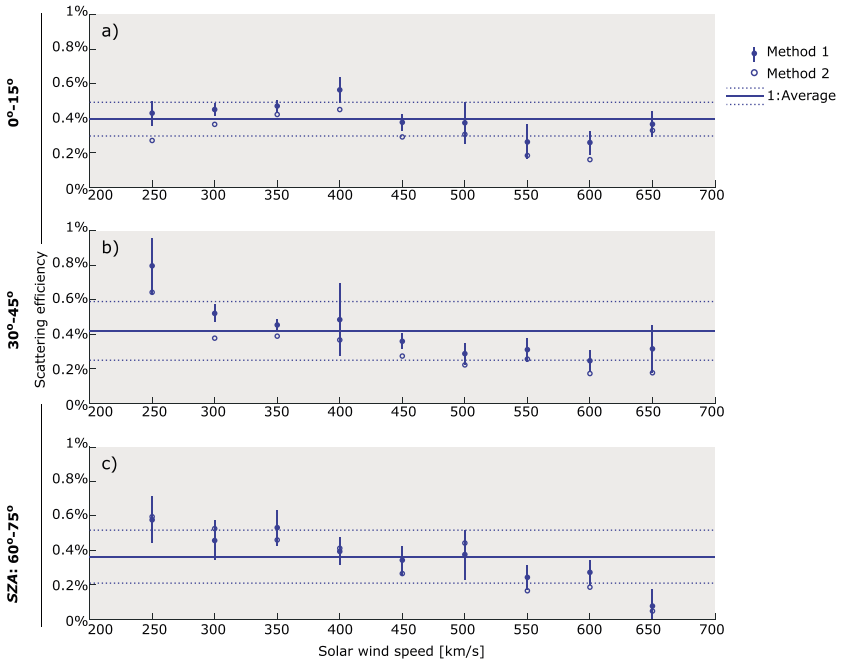

Figure 4. Proton scattering rate versus solar wind speed (v_{sw}) and solar-zenith angle (*SZA*), with a v_{sw}-bin width of 50 km/s, estimated in two different ways (see Section 4). The error bars shown for Method 1 represent the standard error of the mean based on measurement variance. The horizontal lines show the results from Method 1, averaged over the nine v_{sw} bins, where the dotted horizontal lines represent the standard-error of the mean.

there are several outliers that are inconsistent with the model results. These outliers likely arise from contamination from other ion populations and do not necessarily indicate a failure of the model. The data and model results show lower peak energies than the L2014 model. The latter model may be affected by observation bias and shifted spectra due to the lack of ion tracing in their analysis, see discussion in the next section.

In Figure 6, we study the properties of the refitted spectrum models further. In Figure 6a, we look at the H^+/H_{ENA} ratio (i.e., the charge-state fraction of scattered particles) as a function of exit speed and impact speed. The positive charge state fraction increases by more than an order of magnitude per 200-km/s increase in exit speed. On the other hand, the charge ratio for a specific exit speed decreases by about an order of magnitude per 200-km/s increase in impact speed. Figure 6b shows that these counteracting trends result in a trend of decreasing total scattering efficiency with impact speed. The scattering efficiency decreases from 0.5–0.6% at

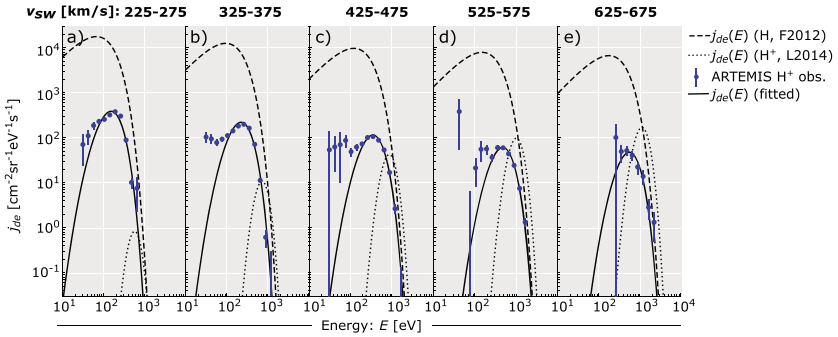

Figure 5. Scattered proton energy spectra as in Figures 1 and 2, for a single solar zenith angle bin of 0°–75° and five solar wind speed (v_{sw}) bins. Also plotted are the empirical models for neutral hydrogen from Futaana et al. (2012; F2012), for protons from Lue et al. (2014; L2014) and the L2014 model refitted to the ARTEMIS observations.

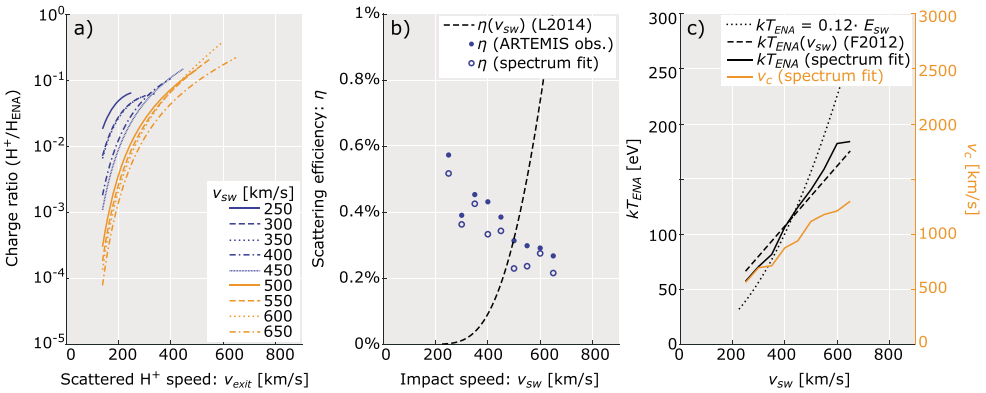

Figure 6. Analysis of the fitted spectrum model results and parameter results. Panel (a) shows the model results for the charge-state fraction as a function of exit speed and impact speed, calculated from the scattered H^+ spectrum divided by the scattered H_{ENA} energy spectrum, given by the spectrum model from Futaana et al. (2012). Panel (b) shows the model results (spectrum fit) for the H^+ scattering efficiency, compared with trapezoidal integration of the observations (ARTEMIS) and the model from Lue et al. (2014; L2014). Panel (c) shows the fitted model parameters kT_{ENA} and v_c, compared with the model for kT_{ENA} (v_{sw}) from Futaana et al. (2012; F2012). A curve corresponding to $kT_{ENA} = 0.12 \cdot E_{sw}$ (where E_{sw} is the solar wind energy) is also plotted for reference.

250–300 km/s to 0.2–0.3% at 600–650 km/s. This negative trend with increasing solar wind speed (also identified in the incidence-angle separated results of Figure 4) is remarkably different to the previously reported positive trend (Lue et al., 2014), shown for reference in Figure 6b. We suspect that the previous results are affected by observation bias. We discuss this discrepancy further in the next section.

The spectral shape parameters of the refitted models are shown in Figure 6c. The v_c values increase with impact speed, from ~600 to ~1,300 km/s for impact speeds (v_{sw}) of 250 to 650 km/s. This trend is in accordance with the trend of decreasing positive fraction with impact speed shown in Figure 6a. The value of v_c = 5,000 km/s given by L2014 was evaluated at v_{sw} = ~550 km/s, but their fitting result was given for an unconstrained scaling factor and are thus not consistent with the H_{ENA} spectrum. The kT_{ENA} values are close to the F2012 model results but increasing faster with solar wind speed. We compare the kT_{ENA} dependence with an energy-proportional dependence $kT_{ENA} = 0.12 \cdot E_{sw}$, where E_{sw} is the solar wind energy. We find the observed trend to be in-between the energy proportionality and velocity proportionality (F2012).

In Figure 7, we collapse the impact speed separation of Figure 3 and show the average directional distributions, allowing impact speeds of 225–675 km/s, for three incidence angle bins (results for three additional bins are available in the supporting information). We compare the results with the H_{ENA} scattering model from Vorburger et al. (2013; V2013) and refit the parameters *z0*, *z1*, *z2*, and *z3* of that model to our results. The refitted model has a clear backward-scattering peak like that of the V2013 model but does not decrease as much in the sideward-scattering direction toward higher *SZA*s as the V2013 model.

5. Discussion

A range of measures have been taken in this study to ensure that the results represent H^+ ions scattered from the lunar surface, without significant contributions from lunar pickup ions (i.e., photo-ionized exospheric species), H^+ from LMAs, or instrument background counts. Although the characteristics of pickup ions (Poppe et al., 2012) and LMA-reflected H^+ (Poppe et al., 2017) in ARTEMIS data have been studied separately, the distinction of the populations in the analysis is not trivial. Nevertheless, the observed characteristics suggest that these methods have been successful.

We observe an energy spectrum that extends to the solar wind energy, peaks at a fraction of this energy, and decreases from there toward lower energies. The spectral shape can be represented by the model given by Lue et al. (2014), although with different fitting parameters obtained in this study. The observed scattering distribution peaks in the backward-scattering direction, like the distribution observed for H_{ENA} (e.g., Vorburger et al., 2013). The results are consistent with the first observations of surface-scattered H^+, including the scattering efficiency of, which was reported as 0.1–1% by Saito et al. (2008).

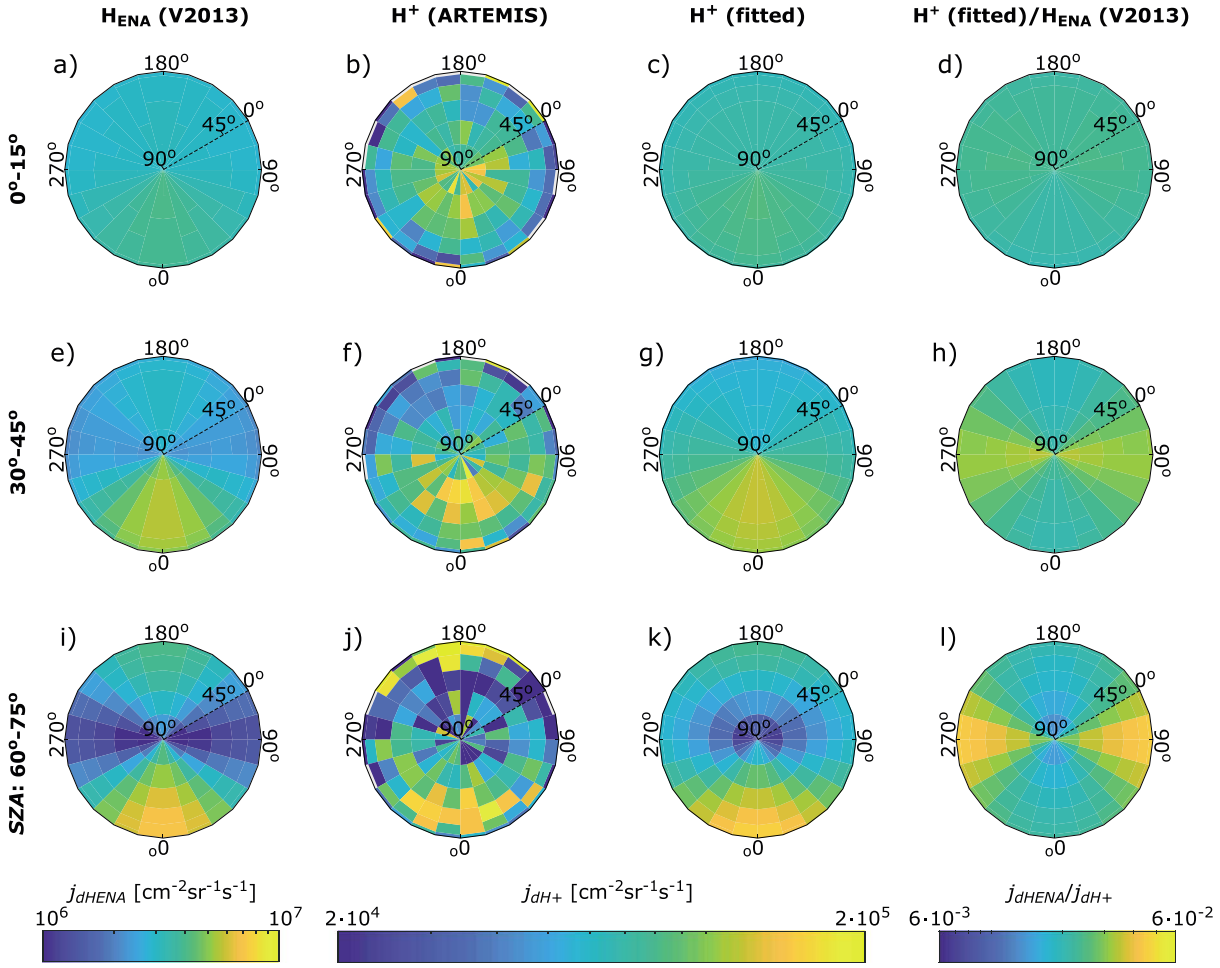

Figure 7. Directional scattering distributions as in Figures 1 and 3, for three solar zenith angle bins. The columns respectively show the empirical model for neutral hydrogen from Vorburger et al. (2013; V2013), the observed proton scattering distribution (including observations for solar wind speeds of 225–675 km/s), the V2013 model refitted to the ARTEMIS observations, and the resulting ratio between the proton and hydrogen models.

However, there is a notable difference in the scattering efficiency's dependence on the solar wind speed between our results and those of Lue et al. (2014; Figure 6b). Lue et al. (2014) found a strong positive correlation between the scattering efficiency and the impact speed, while we observe an opposite trend in the present study. Here we will address this contradiction and provide reasons for why the previous results may have been miscalculated. Lue et al. (2014) did not back trace their observations according to the solar wind magnetic and electric fields. Instead, they assumed a linear trajectory with no significant change in differential flux or energy. Their study was also limited to using a single viewing direction of their detector, which may variably have been favorable or unfavorable to scattered H^+. Furthermore, they placed a strict limitation to the energy bins used, to avoid an instrumental effect at energies just above the solar wind energy. This means that accelerated ions may have been missed. Additionally, they defined a smaller exclusion zone for LMAs than that of the present study. Each of these effects may have affected their results and may have favored detection during higher solar wind speeds and disfavored detection at lower speeds.

The shape of the energy spectrum is similar to the existing model by Lue et al. (2014) but needs to be shifted to lower energies, which can be achieved by decreasing the v_c parameter ("characteristic charge-exchange velocity"). We find that the v_c parameter is not only lower, but variable with the solar wind impact velocity; $v_c \approx 2 \cdot v_{sw}$. While the previous model was based on observations at a solar wind impact speed of 550 km/s, the adjusted model is valid for 250–650 km/s. A characteristic velocity v_c near the Bohr velocity of 2,300 km/s for the electron in an H atom is reasonable for the charge-exchange process, but the apparent

variability of this parameter is unexpected. We expected two protons that leave the surface at the same speed to have equal probability to leave with a positive charge, without "memory" of its initial impact speed (c.f. Wieser et al., 2002). In this case, the v_c parameter would be a constant. However, our results suggest that the charge state is decided over the course of the path inside the surface material, where a proton that had a higher impact speed, experienced more collisions, and traveled a longer path in the surface (to reach the same exit speed as the other) apparently has a higher tendency to leave as neutral hydrogen. On the other hand, we note that our comparison between H_{ENA} and H^+, which is implied in our usage of the v_c parameter, is sensitive to the spectral shape and quantity of the scattered H_{ENA}. The H_{ENA} spectrum is relatively uncertain at high exit energies due to the energy resolution of the observations behind the H_{ENA} model (Futaana et al., 2012). Further, a quantitative decrease in the H_{ENA} scattering rate with solar wind speed has been reported by Funsten et al. (2013; from 20% to 8%), though the same effect was not observed by Futaana et al. (2012). Qualitatively, such a decrease could explain the decreasing trend that we observe, but quantitatively, it is not sufficient because we observe a more than two orders-of-magnitude decrease between the curve for 250- and 650-km/s solar wind speed in Figure 6a.

When we fitted the L2014 spectrum function, we allowed the kT_{ENA} parameter to be fitted instead of fixing it at the (F2012) values given for H_{ENA}. Futaana et al. (2012) found that kT_{ENA} is proportional to the solar wind impact speed as kT_{ENA} (eV) = 0.273·v_{sw} (km/s)—1.99. They discussed that this finding was unexpected as they would have expected a linear dependence on the impact energy. We propose a hypothesis to explain this behavior. The explanation would be that the width of the total energy spectrum increases linearly with impact energy, but because an increasing amount becomes positively charged at higher exit energies, the H_{ENA} spectrum width only increases in proportion to the square root of the impact energy. When we compare our kT_{ENA} results as a function of impact speed (Figure 6c) with the velocity-proportionality from F2012 and an energy-proportional curve, we find our results in-between these dependencies. Thus, our results are not sufficient to prove our hypothesis. As in the preceding paragraph, we note that this test is highly sensitive to the shape of the H_{ENA} spectrum at high exit energies.

The finding that the scattering function is similar between H_{ENA} and H^+ supports the conclusion that these observations are indeed of the same phenomenon (i.e., surface scattering). At nonnormal incidence angles, this scattering is observed to be mainly backward-oriented as opposed to the forward-oriented reflection/deflection from LMAs (Fatemi et al., 2014; Poppe et al., 2017). The favoring of the backward direction is also consistent with simulations of scattering off lunar regolith particles (Starukhina, 2003). Our results are different from the H_{ENA} results in that our scattering function has a larger uniform component at high scattering angles and a smaller forward-directed component. Thus, the "*f1*" component that captures this effect in the V2013 model can be set to unity, which is equivalent to setting the fitting parameter *z1* = 0. On the other hand, we note that the data that our model is fitted to have a high variance and that there might be a forward-directed component at high *SZA* that the model fitting does not capture (see Figures 7j and 7k).

6. Conclusions

We have addressed H^+ scattering off lunar regolith in a statistical study using ARTEMIS data to follow up on first observations (Saito et al., 2008) from Kaguya data and characterization efforts (Lue et al., 2014) based on Chandrayaan-1 data.

Our results suggest that the existing model for the shape of the scattered H^+ energy spectrum (Lue et al., 2014) should be modified, with $v_c \approx 2 \cdot v_{sw}$. Thereafter, the model can be applied to the solar wind velocity range of 250–650 km/s, and 0°–75° *SZA*.

We find that the existing model for the directional distribution of scattered H_{ENA} (Schaufelberger et al., 2011; Vorburger et al., 2013) is applicable also to surface-scattered H^+ (for 250–650 km/s solar wind speed, and 0°–75° *SZA*) but the parameter *z1* can be set to 0 to better represent the observed H^+ scattering at 60°–75° *SZA*.

We find that the previously reported rapid decrease of the H^+ scattering efficiency with decreasing solar wind impact speed likely is false, perhaps due to overreduction of noise signals and the lack of ion tracing between the spacecraft and the surface. Instead, our new results show a decreasing scattering efficiency from 0.5% at $v_{sw} \approx 300$ km/s to 0.3% at $v_{sw} \approx 600$ km/s. The scattering efficiency appears to be the result of two counteracting effects of increasing impact speed, where the probability of a positive charge state of a scattered

particle increases due to the increasing exit speed from the surface but decreases due to the increasing entry speed into the surface. The latter dependence remains to be explained.

The differences between the H_{ENA} and H^+ properties point to intriguing aspects of particle-surface interaction physics. Future studies are needed to understand the charge-state dynamics involved and to provide a picture of H^+ scattering that is consistent between observations from multiple spacecraft (ARTEMIS, Chandrayaan-1, Chang'E-1, Chang'E-2, and Kaguya) that each have different viewing conditions, instrument background levels, species distinction, orbits, and solar wind parameter coverage.

Acknowledgments
This study was supported by NASA's Lunar Data Analysis Program, grant NNX15AP89G. We thank V. Angelopoulos and NASA contract NAS5-02099 for the operation of the ARTEMIS mission. We thank K. -H. Glassmeier, U. Auster, and W. Baumjohann for the Flux Gate Magnetometer data provided under the lead of the Technical University of Braunschweig and with financial support through the German Ministry for Economy and Technology and the German Center for Aviation and Space (DLR), contract 50 OC 0302. The study benefited from collaboration within ISSI (International Space Science Institute) International Team 336. The ARTEMIS data used in this study are publicly available at NASA's CDAWeb (https://cdaweb.sci.gsfc.nasa.gov) and the ARTEMIS mission site (http://artemis.ssl.berkeley.edu). The authors thank Larissa Starukhina and one anonymous reviewer for comments that greatly improved the analysis, presentation, and interpretation of the results of this study.

References

Angelopoulos, V. (2010). The ARTEMIS mission. In C. Russel, & V. Angelopoulos (Eds.), *The ARTEMIS Mission* (pp. 3–25). New York, NY: Springer. https://doi.org/10.1007/978-1-4614-9554-3_2

Auster, H. U., Glassmeier, K. H., Magnes, W., Aydogar, O., Baumjohann, W., Constantinescu, D., et al. (2009). The THEMIS fluxgate magnetometer. In J. L. Burch, & V. Angelopoulus (Eds.), *The THEMIS mission* (pp. 235–264). New York, NY: Springer. https://doi.org/10.1007/978-0-387-89820-9_11

Deca, J., Divin, A., Lembège, B., Horányi, M., Markidis, S., & Lapenta, G. (2015). General mechanism and dynamics of the solar wind interaction with lunar magnetic anomalies from 3-D particle-in-cell simulations. *Journal of Geophysical Research: Space Physics*, *120*, 6443–6463. https://doi.org/10.1002/2015JA021070

Fatemi, S., Holmström, M., Futaana, Y., Lue, C., Collier, M. R., Barabash, S., & Stenberg, G. (2014). Effects of protons reflected by lunar crustal magnetic fields on the global lunar plasma environment. *Journal of Geophysical Research: Space Physics*, *119*, 6095–6105. https://doi.org/10.1002/2014JA019900

Funsten, H. O., Allegrini, F., Bochsler, P. A., Fuselier, S. A., Gruntman, M., Henderson, K., et al. (2013). Reflection of solar wind hydrogen from the lunar surface. *Journal of Geophysical Research: Planets*, *118*, 292–305. https://doi.org/10.1002/jgre.20055

Futaana, Y., Barabash, S., Wieser, M., Holmström, M., & Bhardwaj, A. (2006). Low energy neutral atoms imaging of the moon. *Planetary and Space Science*, *54*(2), 132–143. https://doi.org/10.1016/j.pss.2005.10.010

Futaana, Y., Barabash, S., Wieser, M., Holmström, M., Bhardwaj, A., Dhanya, M. B., et al. (2010). Protons in the near-lunar wake observed by the sub-keV atom reflection analyzer on board Chandrayaan-1. *Journal of Geophysical Research*, *115*, A10248. https://doi.org/10.1029/2010JA015264

Futaana, Y., Barabash, S., Wieser, M., Holmström, M., Lue, C., Wurz, P., et al. (2012). Empirical energy spectra of neutralized solar wind protons from the lunar regolith. *Journal of Geophysical Research*, *117*, E05005. https://doi.org/10.1029/2011JE004019

Futaana, Y., Barabash, S., Wieser, M., Lue, C., Wurz, P., Vorburger, A., et al. (2013). Remote energetic neutral atom imaging of electric potential over a lunar magnetic anomaly. *Geophysical Research Letters*, *40*, 262–266. https://doi.org/10.1002/grl.50135

Futaana, Y., Machida, S., Saito, Y., Matsuoka, A., & Hayakawa, H. (2003). Moon-related nonthermal ions observed by Nozomi: Species, sources, and generation mechanisms. *Journal of Geophysical Research*, *108*(A1), 1025. https://doi.org/10.1029/2002JA009366

Halekas, J. S., Poppe, A. R., Farrell, W. M., Delory, G. T., Angelopoulos, V., McFadden, J. P., et al. (2012). Lunar precursor effects in the solar wind and terrestrial magnetosphere. *Journal of Geophysical Research*, *117*, A05101. https://doi.org/10.1029/2011JA017289

Halekas, J. S., Poppe, A. R., Lue, C., Farrell, W. M., & McFadden, J. P. (2017). Distribution and solar wind control of compressional solar wind-magnetic anomaly interactions observed at the Moon by ARTEMIS. *Journal of Geophysical Research: Space Physics*, *122*, 6240–6254. https://doi.org/10.1002/2017JA023931

Halekas, J. S., Poppe, A. R., McFadden, J. P., Angelopoulos, V., Glassmeier, K.-H., & Brain, D. A. (2014). Evidence for small-scale collisionless shocks at the Moon from ARTEMIS. *Geophysical Research Letters*, *41*, 7436–7443. https://doi.org/10.1002/2014GL061973

Harada, Y., Futaana, Y., Barabash, S., Wieser, M., Wurz, P., Bhardwaj, A., et al. (2014). Backscattered energetic neutral atoms from the Moon in the Earth's plasma sheet observed by Chandarayaan-1/sub-keV atom reflecting analyzer instrument. *Journal of Geophysical Research: Space Physics*, *119*, 3573–3584. https://doi.org/10.1002/2013JA019682

Holmström, M., Wieser, M., Barabash, S., Futaana, Y., & Bhardwaj, A. (2010). Dynamics of solar wind protons reflected by the Moon. *Journal of Geophysical Research*, *115*, A06206. https://doi.org/10.1029/2009JA014843

Lue, C., Futaana, Y., Barabash, S., Saito, Y., Nishino, M., Wieser, M., et al. (2016). Scattering characteristics and imaging of energetic neutral atoms from the Moon in the terrestrial magnetosheath. *Journal of Geophysical Research: Space Physics*, *121*, 432–445. https://doi.org/10.1002/2015JA021826

Lue, C., Futaana, Y., Barabash, S., Wieser, M., Bhardwaj, A., & Wurz, P. (2014). Chandrayaan-1 observations of backscattered solar wind protons from the lunar regolith: Dependence on the solar wind speed. *Journal of Geophysical Research: Planets*, *119*, 968–975. https://doi.org/10.1002/2013JE004582

Lue, C., Futaana, Y., Barabash, S., Wieser, M., Holmström, M., Bhardwaj, A., et al. (2011). Strong influence of lunar crustal fields on the solar wind flow. *Geophysical Research Letters*, *38*, L03202. https://doi.org/10.1029/2010GL046215

McComas, D. J., Allegrini, F., Bochsler, P., Frisch, P., Funsten, H. O., Gruntman, M., et al. (2009). Lunar backscatter and neutralization of the solar wind: First observations of neutral atoms from the Moon. *Geophysical Research Letters*, *36*, L12104. https://doi.org/10.1029/2009GL038794

McFadden, J. P., Carlson, C. W., Larson, D., Ludlam, M., Abiad, R., Elliot, B., et al. (2008). The THEMIS ESA plasma instrument and in-flight calibration. *Space Science Reviews*, *141*, 277–302. https://doi.org/10.1007/s11214-008-9440-2

Nishino, M. N., Fujimoto, M., Maezawa, K., Saito, Y., Yokota, S., Asamura, K., et al. (2009). Solar-wind proton access deep into the near-Moon wake. *Geophysical Research Letters*, *36*, L16103. https://doi.org/10.1029/2009GL039444

Poppe, A. R., Halekas, J. S., Lue, C., & Fatemi, S. (2017). ARTEMIS observations of the solar wind proton scattering function from lunar crustal magnetic anomalies. *Journal of Geophysical Research: Planets*, *122*, 771–783. https://doi.org/10.1002/2017JE005313

Poppe, A. R., Samad, R., Halekas, J. S., Sarantos, M., Delory, G. T., Farrell, W. M., et al. (2012). ARTEMIS observations of lunar pick-up ions in the terrestrial magnetotail lobes. *Geophysical Research Letters*, *39*, L17104. https://doi.org/10.1029/2012GL052909

Poppe, A. R., Sarantos, M., Halekas, J. S., Delory, G. T., Saito, Y., & Nishino, M. (2014). Anisotropic solar wind sputtering of the lunar surface induced by crustal magnetic anomalies. *Geophysical Research Letters*, *41*, 4865–4872. https://doi.org/10.1002/2014GL060523

Purucker, M. E., & Nicholas, J. B. (2010). Global spherical harmonic models of the internal magnetic field of the Moon based on sequential and coestimation approaches. *Journal of Geophysical Research*, *115*, E12007. https://doi.org/10.1029/2010JE003650

Saito, Y., Nishino, M. N., Fujimoto, M., Yamamoto, T., Yokota, S., Tsunakawa, H., et al. (2012). Simultaneous observation of the electron acceleration and ion deceleration over lunar magnetic anomalies. *Earth, Planets and Space*, *64*(2), 83–92. https://doi.org/10.5047/eps.2011.07.011

Saito, Y., Yokota, S., Asamura, K., Tanaka, T., Nishino, M. N., Yamamoto, T., et al. (2010). In-flight performance and initial results of Plasma Energy Angle and Composition Experiment (PACE) on SELENE (Kaguya). *Space Science Reviews*, *154*(1–4), 265–303. https://doi.org/10.1007/s11214-010-9647-x

Saito, Y., Yokota, S., Tanaka, T., Asamura, K., Nishino, M. N., Fujimoto, M., et al. (2008). Solar wind proton reflection at the lunar surface: Low energy ion measurement by MAP-PACE onboard SELENE (KAGUYA). *Geophysical Research Letters*, *35*, L24205. https://doi.org/10.1029/2008GL036077

Schaufelberger, A., Wurz, P., Barabash, S., Wieser, M., Futaana, Y., Holmström, M., et al. (2011). Scattering function for energetic neutral hydrogen atoms off the lunar surface. *Geophysical Research Letters*, *38*, L22202. https://doi.org/10.1029/2011GL049362

Sibeck, D. G., Angelopoulos, V., Brain, D. A., Delory, G. T., Eastwood, J. P., Farrell, W. M., et al. (2011). ARTEMIS science objectives. In C. Russell, & V. Angelopoulos (Eds.), *The ARTEMIS mission* (pp. 27–59). New York, NY: Springer. https://doi.org/10.1007/978-1-4614-9554-3_3

Starukhina, L. V. (2003). Computer simulation of sputtering of lunar regolith by solar wind protons: Contribution to change of surface composition and to hydrogen flux at the lunar poles. *Solar System Research*, *37*(1), 36–50. https://doi.org/10.1023/A:1022347821862

Vorburger, A., Wurz, P., Barabash, S., Futaana, Y., Wieser, M., Bhardwaj, A., et al. (2016). Transport of solar wind plasma onto the lunar nightside surface. *Geophysical Research Letters*, *43*, 10,586–10,594. https://doi.org/10.1002/2016GL071094

Vorburger, A., Wurz, P., Barabash, S., Wieser, M., Futaana, Y., Bhardwaj, A., & Asamura, K. (2015). Imaging the south pole-Aitken basin in backscattered neutral hydrogen atoms. *Planetary and Space Science*, *115*, 57–63. https://doi.org/10.1016/j.pss.2015.02.007

Vorburger, A., Wurz, P., Barabash, S., Wieser, M., Futaana, Y., Holmström, M., et al. (2012). Energetic neutral atom observations of magnetic anomalies on the lunar surface. *Journal of Geophysical Research*, *117*, A07208. https://doi.org/10.1029/2012JA017553

Vorburger, A., Wurz, P., Barabash, S., Wieser, M., Futaana, Y., Lue, C., et al. (2013). Energetic neutral atom imaging of the lunar surface. *Journal of Geophysical Research: Space Physics*, *118*, 3937–3945. https://doi.org/10.1002/jgra.50337

Wieser, M., Barabash, S., Futaana, Y., Holmström, M., Bhardwaj, A., Sridharan, R., et al. (2010). First observation of a mini-magnetosphere above a lunar magnetic anomaly using energetic neutral atoms. *Geophysical Research Letters*, *37*, L05103. https://doi.org/10.1029/2009GL041721

Wieser, M., Barabash, S., Futaana, Y., Holmström, M., Bhardwaj, A., Sridharan, R., et al. (2009). Extremely high reflection of solar wind protons as neutral hydrogen atoms from regolith in space. *Planetary and Space Science*, *57*(14–15), 2132–2134. https://doi.org/10.1016/j.pss.2009.09.012

Wieser, M., Wurz, P., Brüning, K., & Heiland, W. (2002). Scattering of atoms and molecules off a magnesium oxide surface. *Nuclear Instruments and Methods in Physics Research B*, *192*(4), 370–380. https://doi.org/10.1016/S0168-583X(02)00486-X

Zimmerman, M. I., Farrell, W. M., & Poppe, A. R. (2015). Kinetic simulations of kilometer-scale mini-magnetosphere formation on the Moon. *Journal of Geophysical Research: Planets*, *120*, 1893–1903. https://doi.org/10.1002/2015JE004865